

Hierarchical Discrete Distribution Decomposition for Match Density Estimation

Zhichao Yin

Trevor Darrell
UC Berkeley

Fisher Yu

Abstract

Existing deep learning methods for pixel correspondence output a point estimate of the motion field, but do not represent the full match distribution. Explicit representation of a match distribution is desirable for many applications as it allows direct representation of the correspondence probability. The main difficulty of estimating a full probability distribution with a deep network is the high computational cost of inferring the entire distribution. In this paper, we propose Hierarchical Discrete Distribution Decomposition, dubbed HD³, to learn probabilistic point and region matching. Not only can it model match uncertainty, but also region propagation. To achieve this, we estimate the hierarchical distribution of pixel correspondences at different image scales without multi-hypotheses ensembling. Despite its simplicity, our method can achieve competitive results for both optical flow and stereo matching on established benchmarks, while the estimated uncertainty is a good indicator of errors. Furthermore, the point match distribution within a region can be grouped together to propagate the whole region even if the area changes across images.

1. Introduction

Finding dense correspondences between two frames, mainly optical flow and stereo matching, is one of the earliest problems studied in computer vision literature due to the importance of its applications in both low-level image processing, such as video compression, and high-level image understanding, like activity recognition. It is a challenging problem because of the inherently ambiguous nature of texture matching, complicated object motion patterns, and disappearing pixels. Estimating the uncertainty is as important as the correspondences, especially for mission-critical applications and incorporating the matching signals with other sensing information.

Region-level matching, giving region propagation, can also find critical roles in computer vision applications such as video editing. Besides the above-mentioned challenges, regions are also affected by complicated object motion, which leads to 2D shape changes due to perspective projection. Here, we borrow terms from fluid dynamics for clearer description. We call the area increase of the same region

on different frames *dispersion* [35] and the opposite *contraction* [4]. Region dispersion cannot be obtained directly based on displacements of points in that region, even with the displacement uncertainty. However, a point-wise displacement distribution can capture region dispersion with probability attenuation and spreading. The existing works on optical flow do not estimate the full match distribution because of computation intractability or focus on point correspondences.

With the success of deep learning approaches, we now can directly regress the displacements from pairs of images. Feed-forward convolutional networks can produce state-of-the-art point-wise matching directly without global optimization. Consequently, deep learning methods can give more efficient models compared to traditional approaches based on local image descriptor and post-hoc optimization. However, the inherent uncertainty signal is missing in recent deep learning works on optical flow and stereo matching.

Classic early work recognized the uncertainty inherent in the optical flow and proposed probabilistic frameworks [33, 38] to address the shortcoming of point estimates approach. Such models can provide an uncertainty measurement together with the displacement, but these methods typically rely on an assumption of local Gaussian noise models. In stereo matching, because of the smaller search space, it is possible to estimate matching uncertainty from the cost volume in classical approaches. But the computation cost for this is still excessive for high-resolution images, and in general, it is not applicable for optical flow because of the huge 4D matching computation required.

Our goal in this paper is to find a general probabilistic framework suitable for match distribution estimation, with applications in optical flow, stereo matching, and region propagation. We propose to represent the pixel displacement as a distribution with a large support area over the other image. To make the inference tractable, we discretize the distribution based on pixel locations. Besides estimating the displacement based on max posterior, we can also estimate how the motion energy disperses explicitly expressed by the probability distribution.

However, a discrete distribution with large support will

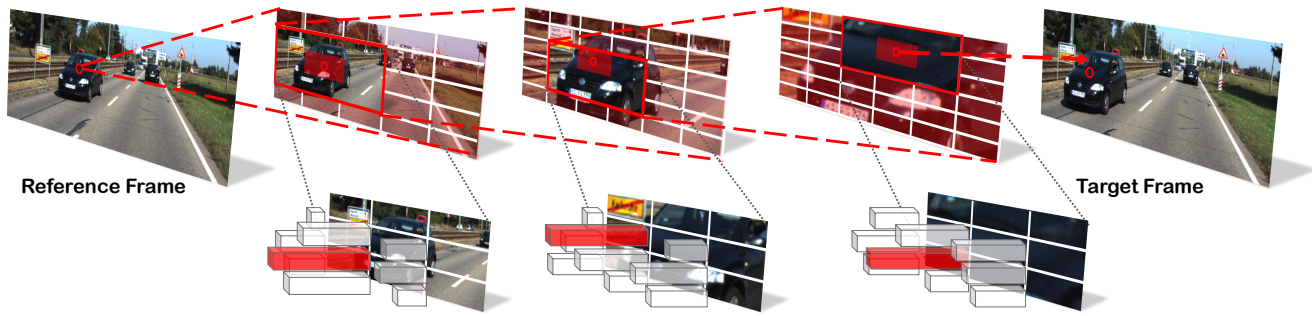


Figure 1: Illustration of HD^3 . We aim to estimate discrete match distribution in this work. For reducing the infeasible computational cost, the overall distribution is decomposed into multiple scales hierarchically at learning time. The full match information can be recovered by aggregating predictions from all levels. Please refer to Sec. 3.2 for more details.

require an infeasible amount of computation. To solve this problem, we propose to decompose the distribution into multiple scales as shown in Fig. 1 and estimate the distributions at the corresponding feature scales. We can learn the distribution hierarchically based on existing deep learning networks which can naturally express the multi-scale information.

The resulting decomposed discrete distribution can not only provide uncertainty estimation directly but also express dispersion for the target regions. The results are applicable for both optical flow and stereo matching. We test our networks on established optical flow and stereo benchmarks based on simulated and real data. Our method can achieve better correspondence accuracy compared to similar networks based on vector estimation. Qualitative results show that the estimated pixel-wise distribution can provide better region propagation and uncertainty estimation.

2. Related Work

The problems of point and region matching are well studied in the optical flow and stereo literature. During the past four decades, a large number of efforts have been devoted to these problems. For a thorough review, we have to refer to KITTI benchmark [27] for the latest advances and Middlebury benchmark [5] for classical methods. Here, we discuss previous works with closely related ideas.

Correspondence optimization Stereo only requires searching correspondences along epipolar lines, which leads to a one-dimensional searching problem where a matching cost volume can be explicitly constructed [31]. The cost volume can be treated as a probabilistic distribution and is closet to our approach. But the computation can still be prohibitive for high-resolution images and stereo matching. Our hierarchical distribution decomposition can compute the matching probability more efficiently. Unfortunately, the search space for optical flow is two

dimensional and the resulting volume space is four dimensional [40]. Therefore, direct displacement vector optimization approaches have been taken since the early development [17]. The optimization has been largely improved since then [6], but uncertainty or displacement distribution is usually not the focus. Our approach aims to predict both dense pixel displacements and their distributions. We make the computation feasible by conceptually decomposing the cost volume in a quadtree fashion.

Classical matching approaches rely on local image descriptors. Due to the lack of context information, they tend to rely on global or semi-global optimization [15]. With the success of convolutional networks in image recognition, the learned image representation has also be introduced to optical flow learning [3, 21]. Because the pixel representation can encode context information, post-hoc optimization seems unnecessary and the deep learning methods adopt regression as the displacement learning strategy, which loses inherent uncertainty information. However, our probabilistic approach can predict the uncertainty directly without turning to other techniques for post-processing [21].

Uncertainty Estimation Probabilistic optical flow has attracted great research interest [33, 38] due to the aperture problem, lumination change, low texture contract, image noise. The common approach is to assume Gaussian noise and pass the noise model through the optimization framework for uncertainty estimation. However, this kind of noise models has small support and assumes constant noise everywhere, which is not true for general region dispersion. Uncertainty can be estimated by multi-hypotheses [21], but the resulting uncertainty can hardly capture the whole point propagation distribution. Our method provides dense propagation distribution. It can model region dispersion by probability attenuation.

We can use stereo matching cost volume to obtain a similar probability distribution, but recent stereo works using convolutional networks give up this valuable informa-

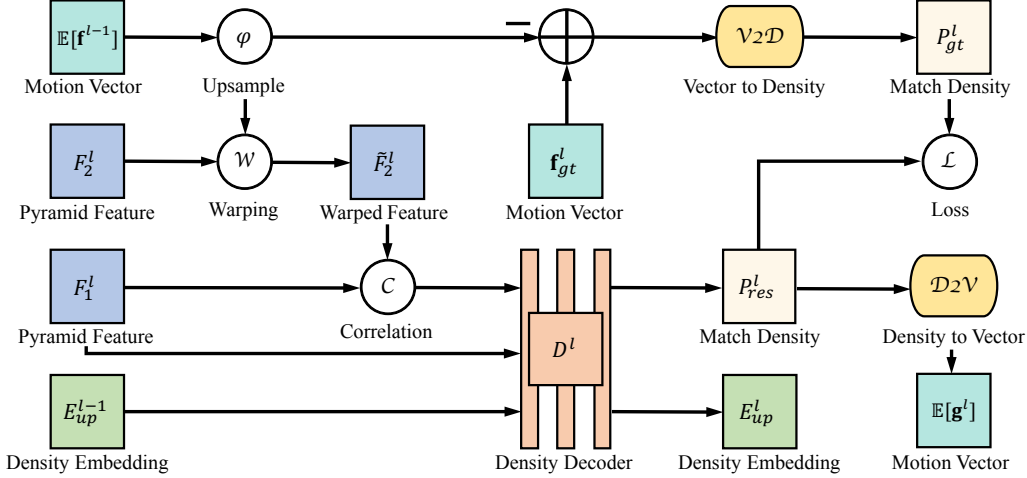


Figure 2: Overview of our architecture. The submodule at the l _{th} level is presented here. F^l and \bar{F}^l denotes the l _{th} level of original and warped pyramid features of image pair I . E_{up}^l denotes upsampled density embeddings between different levels facilitating gradient propagation. \mathbf{f}^l and \mathbf{g}^l denote motion vectors and P^l corresponds to match density. Their conversion is fulfilled by our $\mathcal{D}2\mathcal{V}$ and $\mathcal{V}2\mathcal{D}$ modules. For details please refer to our method part. This figure is best viewed in color.

tion [37, 28, 7]. Xu *et al.* [40] extends the cost volume approach in stereo to optical flow and exploits volume regularity for efficient computation, but the dense probabilistic representation of the volume is lost. Our probabilistic representation can be easily applied to both stereo and optical flow.

Coarse-to-fine Because of the complexity of finding 2D displacements for each pixel in optical flow, it is natural to match the images from coarse to fine in an image or feature pyramid. This is effective in the optimization methods [1, 33, 3] as well as patch matching [18]. This is also used in deep learning approaches such as SpyNet [29], PWC-Net [34] and LiteFlowNet [19]. We use the feature pyramid representation based on Deep Layer Aggregation [43]. Our novelty lies in decomposing the probability distribution at the same time and the scales of the distribution hierarchy are the same as the features on which each probability component is estimated.

3. Method

In this section, we discuss the match density decomposition and our designs for fulfilling this objective. Without loss of generality, we focus on solving 2D correspondences in this part, which can be easily extended into the 1D case.

3.1. Preliminary

We firstly introduce the notations and basic concepts used in this section. Given an image pair $I = \{I_1, I_2\}$, for any pixel coordinate \mathbf{x}_i in I_1 , classical motion field gives its correspondence in I_2 as $\mathbf{x}_i + \mathbf{f}_i$. Different from Wannenwetsch *et al.* [38], where $\{\mathbf{f}_i\}$ are continuous variables,

we treat $\{\mathbf{f}_i\}$ as discrete random variables, the density functions of which are named as **match densities**. The support of \mathbf{f}_i is defined as $R_i = \{\mathbf{d} \in \mathbb{Z}^2 : P(\mathbf{f}_i = \mathbf{d} | I) > 0\}$. We further denote the set of $\{\mathbf{f}_i\}$ by \mathbf{f} and the joint distribution $P(\{\mathbf{f}_i\} | I)$ by $P(\mathbf{f} | I)$. For brevity, we omit prior I in the following sections. Lastly, we introduce an upsampling operator of \mathbf{f} followed by scaling the magnitude of each \mathbf{f}_i by 2, the combination of which we denote by φ . Similarly, we denote the opposite downsampling operator by φ^{-1} .

3.2. Match Density Decomposition

The main challenge of estimating the general match density is the prohibitive computational cost. Assuming the image size is 1000×1000 and the displacement range is $[-50, 50]$. The cardinality of $\{\mathbf{f}_i\}$ is 10^6 and the support size $|R_i|$ of each \mathbf{f}_i can be 10^4 . Therefore the entire distribution volume has 10 billion cells, which is intractable to generate.

Our key observation is that the volume can be decomposed hierarchically into multiple level distributions. An intuitive illustration is depicted in Fig. 1. To start with, we consider decomposing \mathbf{f} into multi-scale discrete motion fields $\{\mathbf{f}^l\}$ ($l = 0, \dots, L$) via

$$\mathbf{f}^l = \begin{cases} \lceil \varphi^{-L}(\mathbf{f}) \rceil, & l = 0 \\ \lceil \varphi^{-(L-l)}(\mathbf{f}) - \varphi(\mathbf{f}^{l-1}) \rceil + \varphi(\mathbf{f}^{l-1}), & l > 0, \end{cases} \quad (1)$$

where $\lceil \cdot \rceil$ rounds its operand to the nearest integer, i.e. round half up. We can see \mathbf{f}^L is identical as \mathbf{f} and higher level $P(\mathbf{f}^l)$ has half resolution of lower level $P(\mathbf{f}^{l+1})$. A further transformation $\mathbf{g}^l = \mathbf{f}^l - \varphi(\mathbf{f}^{l-1})$ shifts the multi-scale

motion fields into residual ones. Naturally, we have the decomposition of $P(\mathbf{f})$ as

$$P(\mathbf{f}) = \prod_l P(\mathbf{g}^l | \mathbf{G}^{l-1}), \quad (2)$$

where $\mathbf{G}^{l-1} = \{\mathbf{g}^j\}_{j=0}^{l-1}$. The reason for adopting such transformation lies in the supports $\{R^l\}$ of $\{\mathbf{g}^l\}$ can be limited within a small local neighborhood, *i.e.* the densities $P(\mathbf{g}^l | \mathbf{G}^{l-1})$ (P_{res}^l for short in the following) are highly concentrated, which we will discuss further in Sec. 3.3. Therefore, for maximizing the posterior distribution $P(\mathbf{f})$, we can achieve good approximation via maximizing each of the decomposed densities P_{res}^l .

To recover the entire match density from the decomposition, we can in turn estimate the multi-scale match densities $\{P_{\text{res}}^l\}$, which is fulfilled by our deep networks D^l (see Sec. 3.4). During training time, the downsampled ground-truth motion field \mathbf{f}_{gt}^l can give direct supervision over each decomposed match density at each level. At inference time, sequentially maximizing the decomposed distributions and aggregating multi-scale predictions give us the max posterior estimation of \mathbf{f} .

3.3. Learning Decomposed Match Densities

We have decomposed the overall distribution $P(\mathbf{f})$ into multi-scale match densities $\{P_{\text{res}}^l\}$, which is also our multi-scale learning objective. In this section, we first discuss the supervision of distribution in each level, which characterizes the ground-truth densities. Let us consider a general motion vector $\mathbf{f}_i \in \mathbf{f}$. As stated in Sec. 3.2, we prefer a concentrated distribution P_i , which simplifies the decomposition and provides more discriminability. We can see \mathbf{f}_i uniquely falls into a 2×2 window W_i in the image grid. This inspires us to splat the bilinear weights of \mathbf{f}_i w.r.t. coordinates in W_i to P_i . Concretely, for any $\mathbf{d} \in \mathbb{Z}^2$, we let

$$P_i(\mathbf{f}_i = \mathbf{d}) = \begin{cases} 0 & \mathbf{d} \notin W_i \\ \rho(\mathbf{f}_i - \tilde{\mathbf{d}}) & \mathbf{d} \in W_i, \end{cases} \quad (3)$$

where $\rho(\cdot)$ means the product of elements in the vector, and $\tilde{\mathbf{d}}$ is the diagonal opposite coordinate of \mathbf{d} in W_i . We call such conversion as $\mathcal{V}2\mathcal{D}$ (see Fig. 3), which is adopted in our ground-truth distribution generation for $\{P_{\text{res}}^l\}$.

As can be seen from Eq. 3, the support of P_i is indeed W_i which has a maximum size of 4. Ideally, we can sample $\{\mathbf{g}^l\}$ in a quadtree fashion from $\{P_{\text{res}}^l\}$, while such computation is still huge for both training and evaluation. For trade-off we can discard samplings with minor probabilities. A natural practice is always taking $\arg \max$ in each level. While we further propose *local expectation* as substitution with less loss of information. Specifically, for any general match density P_i , we define $W_i^* \subseteq R_i$ as the 2×2 window where the integral of P_i over W_i^* maximizes

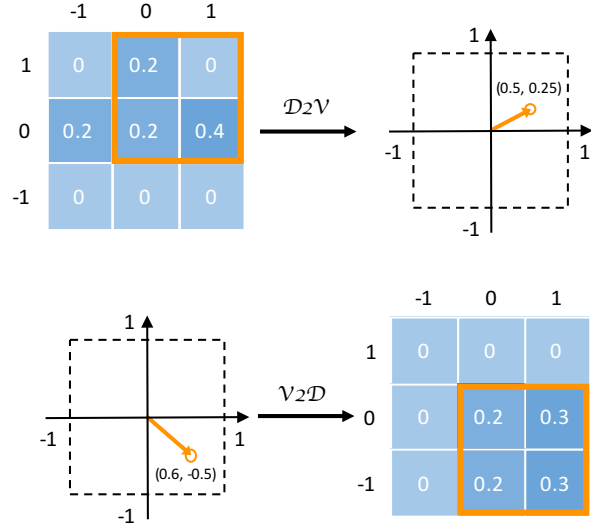


Figure 3: Conversion between motion vectors and match densities. The support is taken as 3×3 here for illustration.

among all candidate windows. We discard probabilities not in W_i^* and normalize P_i over W_i^* into P_i^* . The *local expectation* is defined as $\mathbb{E}[\mathbf{f}_i]$ w.r.t. P_i^* . In the following, we use expectation to denote local expectation by default. We call such conversion as $\mathcal{D}2\mathcal{V}$ (see Fig. 3). Thereby at each level, instead of exhaustive sampling, we always take the max posterior of \mathbf{g}^l as $\mathbb{E}[\mathbf{g}^l]$, and we are literally always learning $P(\mathbf{g}^l | \mathbf{G}^{(l-1)*})$ in each level, where $\mathbf{G}^{(l-1)*}$ is the local expectations of \mathbf{G}^{l-1} . Aggregating max posterior estimations from each level produces our estimation of \mathbf{f} .

3.4. Network Architecture Design

Finally, we discuss the network architecture design fulfilling decomposed match density learning. We achieve this objective via stacking a chain of deep networks, which we call density decoders $\{D^l\}$. At each level, D^l takes charge of inferring the match density P_{res}^l in the respective level. A single level of the entire network is illustrated in Fig. 2. In the following, we discuss the details of our subnetworks.

The crucial spirit in our design of density decoder D^l lies in the targeted output P_{res}^l is closely related with the similarity information between image pair, or their embedded representations. Therefore we impose our match density estimation upon multi-scale feature embeddings $\{F_1^l, F_2^l\}$, which can be extracted via a DLA [43] network over $\{I_1, I_2\}$ respectively. The affinity information can be obtained through the correlation [9] between feature embeddings of different frames. For performing long-range correlation and imposing conditional priors from previous levels, we always warp the feature F_2^l according to $\varphi(\mathbb{E}[\mathbf{f}^{l-1}])$ before correlation. The cost volume is concatenated with

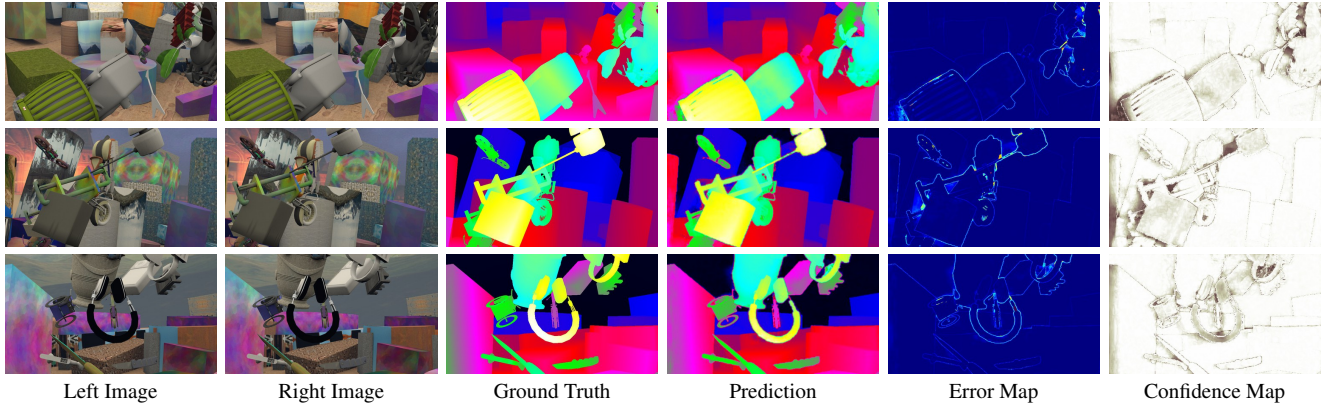


Figure 4: Visualized stereo results on the test split of FlyingThings3D dataset. Cold colors in the error map denote correct predictions while warm colors mean the contrary. Our network gives accurate results in most regions, while errors mainly concentrate on boundaries.

F_1^l and upsampled density embedding E_{up}^{l-1} from previous level, then fed into our density decoder D^l . The decoder D^l is fulfilled via a preactivated HDA [14, 43], producing the density embedding upon which we obtain the match density via a classifier. Finally, for facilitating the gradient propagation, we upsample the density embedding to E_{up}^l and feed it into the next level as density bypass.

During training time, we downsample the full-resolution ground-truth motion field into \mathbf{f}_{gt}^l . The residual motion w.r.t. to $\varphi(\mathbb{E}[\mathbf{f}^{l-1}])$ is converted into P_{gt}^l . While predicted match density P_{res}^l from density decoder D^l is converted into motion vector $\mathbb{E}[\mathbf{g}^l]$. The entire training loss comes in the form of Kullback–Leibler divergence

$$\mathcal{L} = \sum_l \sum_{\mathbf{d} \in R^l} P_{\text{gt}}^l(\mathbf{d})(\log P_{\text{gt}}^l(\mathbf{d}) - \log P_{\text{res}}^l(\mathbf{d})). \quad (4)$$

4. Experiments

HD^3 provides hierarchically decomposed match densities. It can be used for different tasks, such as stereo matching and optical flow. The probability of those vectors can be used as uncertainty estimation. It is hard to directly evaluate the quality of the learned distribution, but we can investigate its performance being applied to these specific tasks.

4.1. Implementation Details

Networks for Variant Tasks We experiment with our models in stereo matching and optical flow. The networks are called HD^3S and HD^3F respectively. HD^3S actually tackles stereo matching as 1D flow estimation. The network designs of these two variants share the most similar spirits but differ slightly: we adopt 1D correlation for HD^3S while 2D correlation for HD^3F . The correlation range is always 4 for both tasks at different levels, which is consistent with the size of match density support. Due to the particularity

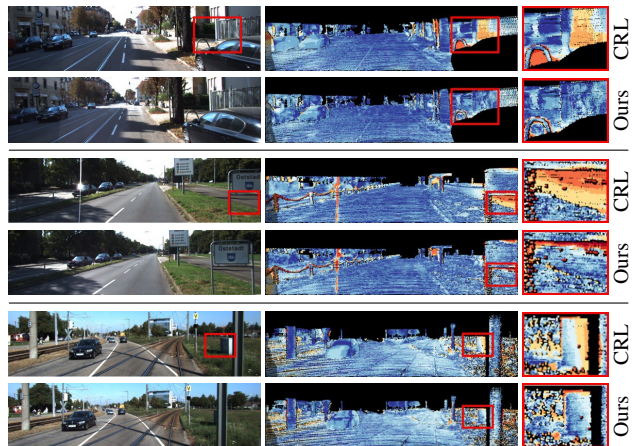


Figure 5: Example stereo error maps on KITTI 2015 test set. We compare our method with CRL [28]. As can be seen in the error maps, our method performs better in fine structures and even occluded area.

of stereo disparity, we clip the 1D flow values larger than 0 in predictions at each level for HD^3S .

Module Details We have two options for the pyramid feature extractor: DLA-34 and DLA-34-Up [43]. The names of models based on DLA-34-Up will be extended with “-Up” suffix. The coarsest level feature embeddings are $\times 64$ downsampled. The density decoder D^l consists of two residual blocks and one aggregation node. We adopt batch normalization [22] in all of our models for stabilizing the training. Empirically, the pyramid level is set to be 5 and 6 for HD^3F and HD^3S respectively. We upsample predictions from the lowest level to full resolution during evaluation.

Training Details In the following we discuss the training schedule of DLA-34 based models, which can be similarly

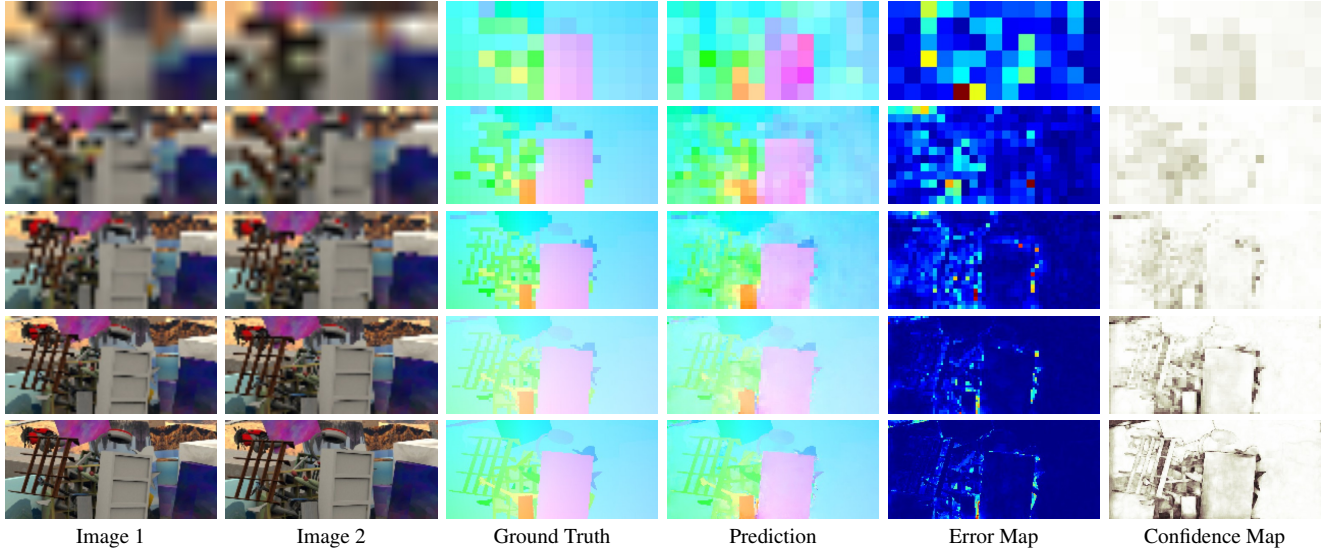


Figure 6: Qualitative multi-scale flow result on the test split of FlyingThings3D dataset. Bilinearly downsampled raw images, coarser level flows, error maps and confidence maps are enlarged via nearest neighbor upsampling for visualization purpose. Our network gives precise predictions in most regions, while presents confusion in occluded regions and disappearing parts.

applied to other ones. Unless otherwise stated, we train our models on 8 GPUs without synchronized batch normalization. The pyramid feature extractor is initialized from ImageNet pretrained weights. The network is optimized by Adam [24], where $\beta_1 = 0.9$, $\beta_2 = 0.999$. The ground-truth is bilinearly downsampled for dense annotations while average pooled for sparse ones. In this section, confidence maps are obtained through aggregating the probabilities within the 2×2 window in our $D2V$ of the last level match density, and uncertain maps are the opposite.

4.2. Stereo Matching Result

To evaluate the performance of our HD³S model, we benchmark our result on the popular KITTI stereo dataset [11]. Due to the limited amount of training data in KITTI, we pretrain our model on the synthetic FlyingThings3D dataset [25].

FlyingThings3D As noticed by recent work [28], the FlyingThings3D dataset suffers from the problem that some images have very large (up to 10^3) or negative disparities. Therefore we follow the training/validation splits of Pang *et al.* [28], which filter some extremely problematic samples. We train our HD³S model with a batch size of 32. The image crop size is 512×896 . We set the initial learning rate as $2e-4$, which we decay by 0.5 every 30 epochs after 70 epochs. Such learning rate decay schedule is adopted in all of our experiments (stereo & optical flow) in synthetic datasets (FlyingChairs & FlyingThings3D). The network is trained for 200 epochs in total. We do not perform data augmentation except for random cropping. For we use the

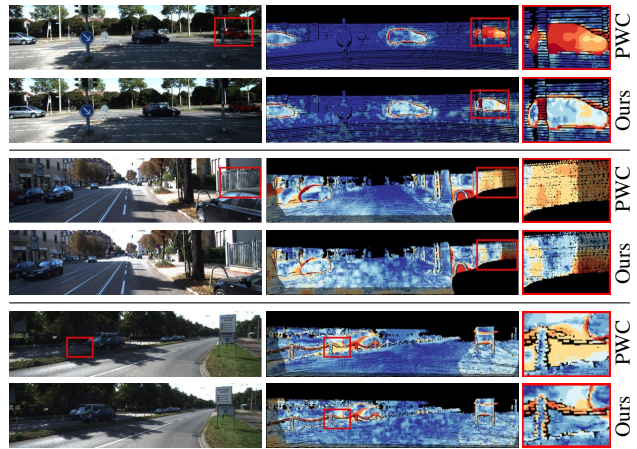


Figure 7: Example flow error maps on the official KITTI 2015 test set. We compare our method with PWC-Net [34]. Our network gives more superior performance in challenging cases, though exhibits certain confusion but without loss of accuracy.

same splits as Pang *et al.* [28], we provide quantitative comparisons in Tab. 1 against other baselines in the test split of FlyingThings3D. As can be seen, our method achieves the lowest end-point-error and second best 3-pixel-error. Qualitative example predictions are shown in Fig. 4.

KITTI During finetuning stage, we combine the available 394 image pairs from KITTI 2012 & 2015 as training data. The batch size is 16 and we train our model on 4 GPUs. Considering the scarcity of training data in KITTI, we perform multi-scale cropping with a crop size of 320×896 .

Metric	SGM [16]	SPS-St [41]	MC [44]	DispNetC [25]	CRL [28]	Ours
EPE	4.50	3.98	3.79	1.84	1.32	1.08
3PE	12.54	12.84	13.70	9.67	6.20	6.40

Table 1: Stereo matching results on the test split [28] of FlyingThings3D. EPE means end-point-error, while 3PE means percentage of pixels for which the prediction error is more than 3 pixels.

Methods	Noc			All		
	D1-bg	D1-fg	D1-all	D1-bg	D1-fg	D1-all
SPS-st [41]	3.50	11.61	4.84	3.84	12.67	5.31
DispNetC [25]	4.11	3.72	4.05	4.32	4.41	4.34
MC-CNN [44]	2.48	7.64	3.33	2.89	8.88	3.89
Displets v2 [13]	2.73	4.95	3.09	3.00	5.56	3.43
L-ResMatch [32]	2.35	5.74	2.91	2.72	6.95	3.42
DRR [12]	2.34	4.87	2.76	2.58	6.04	3.16
GC-Net [23]	2.02	5.58	2.61	2.21	6.16	2.87
CRL [28]	2.32	3.12	2.45	2.48	3.59	2.67
HD ³ S (Ours)	1.88	4.90	2.38	2.12	5.40	2.67
HD ³ S-Up (Ours)	1.84	4.84	2.33	2.06	5.47	2.63

Table 2: Stereo matching results on KITTI 2015 test set over non-occluded regions (Noc) and overall regions (All). All of the numbers mean percentage of pixels with errors of more than three pixels or 5% of disparity magnitude.

The scale is uniformly sampled from $[0.5 \sim 1.15]$. Also, we adopt the same color augmentation as Meister *et al.* [26] but without Gaussian blur. Based on the pretrained model on FlyingThings3D, we set the initial learning rate as $1e-5$ and decay by 0.5 at 1000 epochs and 1500 epochs respectively. The network is trained for 2000 epochs in total. Benchmark result on KITTI 2015 is demonstrated in Tab. 2. Again, our method achieves better results than competitive baselines. Note that our HD³S-Up has only 38.6M parameters and takes 112 ms to process a standard KITTI stereo pair, while CRL [28] has 81.1M parameters and its inference time is 470ms. Sample predictions are shown in Fig. 5.

4.3. Optical Flow Result

To validate the effectiveness of our model in optical flow, we experiment with synthetic datasets including FlyingChairs [9] and FlyingThings3D [25], and real-world dataset KITTI [11].

FlyingChairs We firstly train our network on FlyingChairs as bootstrap. The batch size is 64 and we directly feed the entire 384×512 images into the network during training for we find large crop size brings more contextual information and better performance. The initial learning rate is 4×10^{-4} . The training loss typically converges after 200 epochs.

FlyingThings3D Based on the pretrained model on Fly-

Methods	KITTI 2012			KITTI 2015		
	AEPE	AEPE	F1-Noc	AEPE	F1-all	F1-all
	<i>train</i>	<i>test</i>	<i>test</i>	<i>train</i>	<i>train</i>	<i>test</i>
EpicFlow [30]	-	3.8	7.88%	-	-	26.29%
FullFlow [8]	-	-	-	-	-	23.37%
CPM-flow [18]	-	3.2	5.79%	-	-	22.40%
PatchBatch [10]	-	3.3	5.29%	-	-	21.07%
FlowFields [3]	-	-	-	-	-	19.80%
MRFlow [39]	-	-	-	-	14.09%	12.19%
DCFlow [40]	-	-	-	-	15.09%	14.83%
SDF [2]	-	2.3	3.80%	-	-	11.01%
MirrorFlow [20]	-	2.6	4.38%	-	9.93%	10.29%
SpyNet-ft [29]	(4.13)	4.7	12.31%	-	-	35.07%
FlowNet2 [21]	4.09	-	-	10.06	30.37%	-
FlowNet2-ft [21]	(1.28)	1.8	4.82%	(2.30)	(8.61%)	10.41%
LiteFlowNet [19]	4.25	-	-	10.46	29.30%	-
LiteFlowNet-ft [19]	(1.26)	1.7	-	(2.16)	(8.16%)	10.24%
PWC-Net [34]	4.14	-	-	10.35	33.67%	-
PWC-Net-ft [34]	(1.45)	1.7	4.22%	(2.16)	(9.80%)	9.60%
HD ³ F (Ours)	(1.07)	1.6	2.55%	(1.83)	(7.46%)	9.75%
HD ³ F-Up (Ours)	(1.08)	1.7	2.67%	(1.57)	(6.40%)	9.52%

Table 3: Optical flow results on KITTI dataset. Numbers of baseline methods are referenced from [19, 34]. AEPE denotes end-point-error while F1 means the percentage of pixels with errors of more than 3 pixels or 5% of flow magnitude. Numbers in parenthesis are results on data the network has been trained on.

ingChairs, we further finetune the model on more complicated FlyingThings3D dataset. We adopt the same subset of FlyingThings3D as [21, 34], which excludes image pairs with extreme motion (magnitude larger than 10^3 pixels). The batch size is 48 due to our selection of a large crop size as 512×896 . The initial learning rate is 6×10^{-5} and we train our model for 140 epochs. We visualize an example multi-scale prediction in Fig. 6. We can see our models refines the predictions from coarse to fine levels. The error maps are positively correlated with the confidence map, which we will discuss further in Sec. 4.4.

KITTI Finally, we finetune our model on KITTI dataset. All available image pairs from KITTI 2012 & 2015 are included for training. All the hyperparameters and augmentations are the same as our stereo experiment in KITTI. We show our benchmark results in Tab. 3. As can be seen, our HD³F achieves state-of-the-art results in the benchmark, demonstrating the effectiveness of our probabilistic method under evaluation metric for motion vectors. We show visualized comparisons against Sun *et al.* [34] in Fig. 7.

4.4. Applications

Finally, we investigate the application of our model into region propagation and uncertainty estimation.

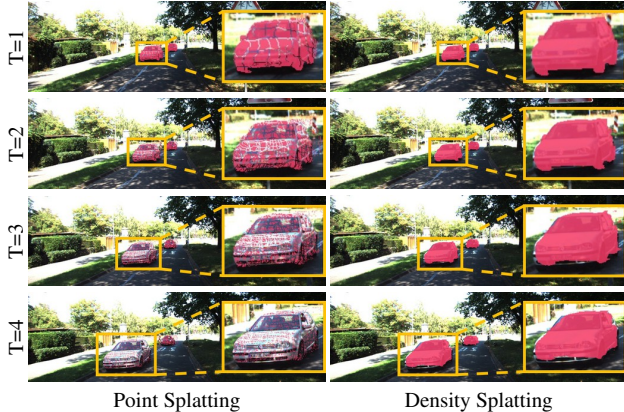


Figure 8: Mask propagation on KITTI dataset. Red indicates points within the propagated foreground mask. Point splatting suffers from the region dispersion issue, while density splatting gives a compact and dense mask across different frames.

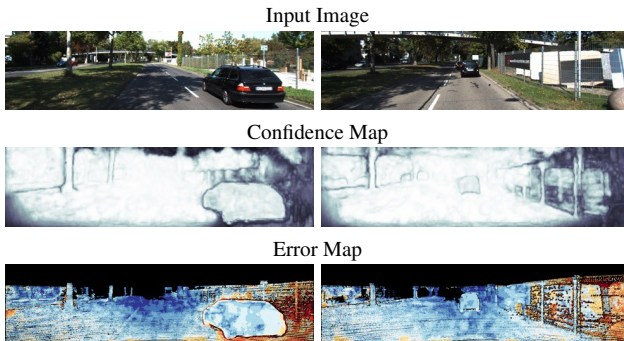


Figure 9: Example confidence maps of our predictions and error maps w.r.t. ground-truth. In confidence maps, white colors mean confident predictions while dark colors denote uncertain ones. In the error maps, warmer colors indicate inaccurate predictions.

Region Propagation For a given segmentation in the first frame, video segmentation algorithms aim to propagate the segmentation from the first frame to the entire video sequence. Directly forward splatting the mask according to point-to-point correspondence may suffer from the *region dispersion* issue: the same physical 3D point may project into different quantities of pixels across video frames due to its relative motion to the camera. As demonstrated in Fig. 8, the first method, namely point splatting, suffers from the region dispersion problem. Due to the car is moving towards the camera, the quantity of points within the mask remains unchanged while the car occupies more and more pixels. Consequently, more and more holes emerge as the car approaches. While in the second column, our density splatting [36] is free from such concern.

Uncertainty Estimation Here we investigate how to measure the reliability of predictions based on our uncertainty

Classes	Methods	Noc		All	
		IoU	Acc	IoU	Acc
Outlier	Consistency	17.5	64.9	23.3	81.9
	Ours	37.6	57.8	44.1	76.4
Inlier	Consistency	84.2	85.8	75.6	76.9
	Ours	96.1	97.8	91.8	93.7
Mean	Consistency	50.9	75.4	49.5	79.4
	Ours	66.9	77.8	68.0	85.1

Table 4: Inlier/outlier prediction classification result on KITTI 2015 training set. Noc denotes evaluation only in the non-occluded area, while All denotes evaluation in the overall region.

map, and compare it with common heuristics for motion vector. Without loss of generality, We take optical flow setting on KITTI dataset for illustration.

Naturally, the per-pixel classification of predictions into correct/wrong ones can be treated as a binary segmentation task. For our probabilistic model, predictions with high uncertainty are more likely to be incorrect. Thus we simply set a threshold σ ($0 < \sigma < 1$), and classify predictions with uncertainty larger (or less) than σ as outliers (or inliers accordingly). In our experiment, we set σ to be 0.3. For comparison, we adopt the forward-backward consistency check for detecting erroneous results. Predictions where the forward and backward flows contradict seriously are treated as outliers. The threshold follows Yin *et al.* [42]. Both methods adopt the same HD³F model for inference.

As can be seen in Tab. 4, criteria provided by our uncertainty gives the highest mean IoU and mean Accuracy in both non-occluded and overall regions. It manifests the positive correlation between our uncertainty estimation and prediction error distribution. A qualitative visualization is shown in Fig. 9. We can see the uncertain cases generally occur at occluded regions when the network has difficulty in finding correspondences and has to hallucinate motion.

5. Conclusion

We propose Hierarchical Discrete Distribution Decomposition (HD³) for estimating full match density. Our approach constructs the matching density hierarchy in parallel with feature pyramids. The predicted density can be converted into displacements, model region propagation by aggregating probability mass transfer, and provide uncertainty estimation. Experiments show that our method achieves very competitive results on established benchmarks.

In the future, we hope to introduce more clues to our framework such as the pixel assignment probabilities from segmentation. In addition, we do not consider relationships between match densities of adjacent pixels in this work, but it can help remove match uncertainty in challenging cases.

References

- [1] P. Anandan. A computational framework and an algorithm for the measurement of visual motion. *IJCV*, 1989. 3
- [2] M. Bai, W. Luo, K. Kundu, and R. Urtasun. Exploiting semantic information and deep matching for optical flow. In *ECCV*, 2016. 7
- [3] C. Bailer, B. Taetz, and D. Stricker. Flow fields: Dense correspondence fields for highly accurate large displacement optical flow estimation. In *ICCV*, 2015. 2, 3, 7
- [4] P. G. Baines. *Topographic effects in stratified flows*. Cambridge university press, 1997. 1
- [5] S. Baker, D. Scharstein, J. Lewis, S. Roth, M. J. Black, and R. Szeliski. A database and evaluation methodology for optical flow. *IJCV*, 2011. 2
- [6] T. Brox and J. Malik. Large displacement optical flow: descriptor matching in variational motion estimation. *PAMI*, 2011. 2
- [7] J.-R. Chang and Y.-S. Chen. Pyramid stereo matching network. In *CVPR*, 2018. 3
- [8] Q. Chen and V. Koltun. Full flow: Optical flow estimation by global optimization over regular grids. In *CVPR*, 2016. 7
- [9] A. Dosovitskiy, P. Fischer, E. Ilg, P. Hausser, C. Hazirbas, V. Golkov, P. Van Der Smagt, D. Cremers, and T. Brox. FlowNet: Learning optical flow with convolutional networks. In *ICCV*, 2015. 4, 7
- [10] D. Gadot and L. Wolf. Patchbatch: a batch augmented loss for optical flow. In *CVPR*, 2016. 7
- [11] A. Geiger, P. Lenz, C. Stiller, and R. Urtasun. Vision meets robotics: The kitti dataset. *IJRR*, 2013. 6, 7
- [12] S. Gidaris and N. Komodakis. Detect, replace, refine: Deep structured prediction for pixel wise labeling. In *CVPR*, 2017. 7
- [13] F. Guney and A. Geiger. Displets: Resolving stereo ambiguities using object knowledge. In *CVPR*, 2015. 7
- [14] K. He, X. Zhang, S. Ren, and J. Sun. Identity mappings in deep residual networks. In *ECCV*, 2016. 5
- [15] H. Hirschmuller. Stereo processing by semiglobal matching and mutual information. *PAMI*, 2008. 2
- [16] H. Hirschmuller and D. Scharstein. Evaluation of stereo matching costs on images with radiometric differences. *PAMI*, 2009. 7
- [17] B. K. Horn and B. G. Schunck. Determining optical flow. *Artificial intelligence*, 1981. 2
- [18] Y. Hu, R. Song, and Y. Li. Efficient coarse-to-fine patch-match for large displacement optical flow. In *CVPR*, 2016. 3, 7
- [19] T.-W. Hui, X. Tang, and C. C. Loy. LiteFlowNet: A lightweight convolutional neural network for optical flow estimation. In *CVPR*, 2018. 3, 7
- [20] J. Hur and S. Roth. Mirrorflow: Exploiting symmetries in joint optical flow and occlusion estimation. In *ICCV*, 2017. 7
- [21] E. Ilg, N. Mayer, T. Saikia, M. Keuper, A. Dosovitskiy, and T. Brox. FlowNet 2.0: Evolution of optical flow estimation with deep networks. In *CVPR*, 2017. 2, 7
- [22] S. Ioffe and C. Szegedy. Batch normalization: Accelerating deep network training by reducing internal covariate shift. In *ICML*, 2015. 5
- [23] A. Kendall, H. Martirosyan, S. Dasgupta, P. Henry, R. Kennedy, A. Bachrach, and A. Bry. End-to-end learning of geometry and context for deep stereo regression. In *ICCV*, 2017. 7
- [24] D. P. Kingma and J. Ba. Adam: A method for stochastic optimization. *CoRR*, 2014. 6
- [25] N. Mayer, E. Ilg, P. Hausser, P. Fischer, D. Cremers, A. Dosovitskiy, and T. Brox. A large dataset to train convolutional networks for disparity, optical flow, and scene flow estimation. In *CVPR*, 2016. 6, 7
- [26] S. Meister, J. Hur, and S. Roth. UnFlow: Unsupervised learning of optical flow with a bidirectional census loss. In *AAAI*, 2018. 7
- [27] M. Menze and A. Geiger. Object scene flow for autonomous vehicles. In *CVPR*, 2015. 2
- [28] J. Pang, W. Sun, J. S. Ren, C. Yang, and Q. Yan. Cascade residual learning: A two-stage convolutional neural network for stereo matching. In *ICCV Workshops*, 2017. 3, 5, 6, 7
- [29] A. Ranjan and M. J. Black. Optical flow estimation using a spatial pyramid network. In *CVPR*, 2017. 3, 7
- [30] J. Revaud, P. Weinzaepfel, Z. Harchaoui, and C. Schmid. Epicflow: Edge-preserving interpolation of correspondences for optical flow. In *CVPR*, 2015. 7
- [31] D. Scharstein and R. Szeliski. A taxonomy and evaluation of dense two-frame stereo correspondence algorithms. *IJCV*, 2002. 2
- [32] A. Shaked and L. Wolf. Improved stereo matching with constant highway networks and reflective confidence learning. In *CVPR*, 2017. 7
- [33] E. P. Simoncelli, E. H. Adelson, and D. J. Heeger. Probability distributions of optical flow. In *CVPR*, 1991. 1, 2, 3
- [34] D. Sun, X. Yang, M.-Y. Liu, and J. Kautz. PWC-Net: CNNs for optical flow using pyramid, warping, and cost volume. In *CVPR*, 2018. 3, 6, 7
- [35] G. I. Taylor. Dispersion of soluble matter in solvent flowing slowly through a tube. *Proc. R. Soc. Lond. A*, 1953. 1
- [36] S. Tulsiani, R. Tucker, and N. Snavely. Layer-structured 3d scene inference via view synthesis. In *ECCV*, 2018. 8
- [37] S. Tulyakov, A. Ivanov, and F. Fleuret. Practical deep stereo (pds): Toward applications-friendly deep stereo matching. *CoRR*, 2018. 3
- [38] A. S. Wannenwetsch, M. Keuper, and S. Roth. Probflow: Joint optical flow and uncertainty estimation. In *ICCV*, 2017. 1, 2, 3
- [39] J. Wulff, L. Sevilla-Lara, and M. J. Black. Optical flow in mostly rigid scenes. In *CVPR*, 2017. 7
- [40] J. Xu, R. Ranftl, and V. Koltun. Accurate optical flow via direct cost volume processing. *CoRR*, 2017. 2, 3, 7
- [41] K. Yamaguchi, D. McAllester, and R. Urtasun. Efficient joint segmentation, occlusion labeling, stereo and flow estimation. In *ECCV*, 2014. 7
- [42] Z. Yin and J. Shi. Geonet: Unsupervised learning of dense depth, optical flow and camera pose. In *CVPR*, 2018. 8

- [43] F. Yu, D. Wang, E. Shelhamer, and T. Darrell. Deep layer aggregation. In *CVPR*, 2018. 3, 4, 5
- [44] J. Zbontar and Y. LeCun. Stereo matching by training a convolutional neural network to compare image patches. *JMLR*, 2016. 7